

Particle–particle drag force in inertial bidisperse gas–particle suspensions

Fan Duan¹, Yaxiong Yu¹, Xiao Chen¹ and Qiang Zhou^{2,†}

¹School of Chemical Engineering and Technology, Xi'an Jiaotong University, Xi'an 710049, PR China

²State Key Laboratory of Multiphase Flow in Power Engineering, Xi'an Jiaotong University, Xi'an 710049, PR China

(Received 17 March 2022; revised 8 August 2022; accepted 12 October 2022)

Particle-resolved direct numerical simulations are employed to investigate the particle–particle drag force in the bidisperse gas–particle suspensions where the particles are smooth and the single-particle velocity distribution function is Maxwellian. The particle Reynolds number ranges from 6.7 to 123.8, and in this range the particle inertia is high enough that the lubrication force is not essential. It is found that the relation derived by the kinetic theory of granular flow (KTGF) highly overestimates the particle–particle drag force. This is because the pre-collision velocities of colliding particles are not completely uncorrelated with each other. From the time sequence of collision events, it is observed that the particle pair that has just collided will probably collide again after a short time due to the restriction of the particle motion in dense suspensions. Since the post-collision velocities of the first collision cannot relax entirely in such a short time, the relative velocity before the subsequent collision is statistically smaller than the domain-averaged relative velocity. Consequently, the particle–particle drag force is over-predicted when the domain-averaged relative velocity is used. For this reason, this work assumes that the particle–particle drag force is determined by the relative velocity within a local region near large particles. When the local region is set to be the spherical shells centred on the centres of large particles and with an outer radius of a mean free path of small particles, the KTGF-based relation can reasonably predict the particle–particle drag force.

Key words: fluidized beds, particle/fluid flows, kinetic theory

1. Introduction

Gas–particle suspensions are widespread in nature and industrial applications. Examples of the former include snowstorms, sandstorms and pyroclastic flows. Typical examples of the latter are fluidized-bed operations for the classification of particles, olefin

† Email address for correspondence: zhou.590@mail.xjtu.edu.cn

polymerization and co-gasification of coal and biomass. In general, the particles contained in these suspensions are polydisperse, which, under the gas–particle drag force and the gravity force, gives rise to relative velocities between particles of different types. For brevity, the relative velocity refers to the velocity difference of different particle types if not otherwise specified. In dense suspensions, the collision frequency between different particle types is high, and the relative velocity is significantly reduced by collisions. The relative velocity is the key characteristic of the segregation phenomenon (Beetstra, van der Hoef & Kuipers 2007; Mehrabadi, Tenneti & Subramaniam 2016; Mehrabadi & Subramaniam 2017). Segregation is desired in the classification of particles, but should be avoided in the process where various particle types need to be well mixed, such as olefin polymerization and co-gasification of coal and biomass. In the literature, the multi-fluid model (MFM) (Iddir & Arastoopour 2005; Chao *et al.* 2011; Zhao & Wang 2021), in which the gas and the particles are treated as interpenetrating continuous phases, is one of the most prevalent methods for studying segregation. In MFM, the transport equations of each particle type are established, and the closure relations are obtained by the kinetic theory of granular flow (KTGF) or by experiments. The gas–particle drag force and the particle–particle drag force are equally crucial to reproducing the segregation phenomenon (Mehrabadi *et al.* 2016). However, studies on the particle–particle drag force are relatively rare. Here, the particle–particle drag force is the mean collision force between different particle types per unit volume. In this paper, the particle–particle drag force is studied by a set of fully resolved methods. The gas flow is resolved to a much smaller scale than the smallest particle diameter, the motion of each particle is tracked by the discrete element method (DEM), and the collisions between particles are simulated by the soft-sphere model (Tsuji, Kawaguchi & Tanaka 1993; Zhu *et al.* 2007; Zhou *et al.* 2010).

In the literature, KTGF is the primary way to obtain the correlation of the particle–particle drag force. The KTGF is based on the classic kinetic theory of gases, which is exhaustively discussed in the book of Chapman & Cowling (1970). The main feature that distinguishes the KTGF from gas is the consideration of the energy dissipation in collisions (Lun *et al.* 1984; Lun 1991; Garzo 2019). Jenkins & Mancini (1987, 1989) first extended the kinetic theory of monodisperse granular flows to binary granular flows. The proposed closure relations, including the relation of the particle–particle drag force, assume the equipartition of the kinetic energy of the peculiar motion, which indicates that the product of the granular temperature and the particle mass is the same for all particle types. Here, the peculiar motion refers to the velocity of a particle relative to the reference frame where the mean velocity of particles is zero. This assumption is strictly valid for a gas in the uniform steady state and not subjected to any external force (Chapman & Cowling 1970), but maybe invalid for granular systems (Feitosa & Menon 2002; Montanero & Garzo 2003; Galvin, Dahl & Hrenya 2005). For this reason, many researchers derived the closure relations of the non-equipartition energy (Iddir & Arastoopour 2005; Songprawat & Gidaspow 2010; Chao *et al.* 2011; Chen, Mei & Wang 2017). To simplify the integral of the collision term, all these relations neglected or partly neglected the relative velocity between different particle types and hence may only apply to the systems where the relative velocity is small compared with the peculiar velocity (Zhao & Wang 2020; Solsvik & Manger 2021). Recently, the closure relations at the first approximation, where the single-particle velocity distribution function (VDF) is assumed Maxwellian, are rigorously derived without any mathematical simplification by Zhao & Wang (2021). Therefore, their relations could apply to the full range of the relative velocity. Unlike the above works, Syamlal (1987) derived a relation for the particle–particle drag force by assuming that all particles of each particle type have

the same velocity. It is worth noting that the relation proposed by Syamlal (1987) is the only particle–particle drag relation that includes the contribution from interparticle friction. Although the mathematical method for the derivation of the particle–particle drag force becomes more and more refined, *a priori* analysis of the obtained relations is still lacking. To the authors' knowledge, only Mehrabadi *et al.* (2016) compared the predictions of the relation proposed by Syamlal (1987) with the data of particle-resolved direct numerical simulations (PR-DNSs). They found that the relation of Syamlal (1987) seriously underestimates the particle–particle drag force due to neglecting the peculiar particle velocity. In this work, PR-DNSs of suspensions containing smooth particles are conducted, and the relation of Zhao & Wang (2021) is examined and improved based on simulation results.

The lubrication force arises when the gap between two approaching particles is very small compared with the particle size and tends to infinity as the gap size decreases to zero in theory. In practice, the growth of the lubrication force is limited by the breakdown of the continuity hypothesis and other reasons. As indicated in Koch (1990), the fractional change in the relative velocity between two approaching particles due to the lubrication force equals $-C/St$. Here, C is a constant of order unity for gas, and the Stokes number, defined as $St = d\rho U_0/(9\mu)$, characterizes the importance of particle inertia. In the expression of St , d , ρ , U_0 and μ represent the particle diameter, the particle mass density, the initial relative velocity between the two approaching particles and the dynamic viscosity of the fluid, respectively. When St is comparable to C , the relative velocity decreases significantly before the collision. As a result, the particle–particle drag force is very small compared with the gas–particle drag force and hence is not important. In the present study, the Stokes number ranges from 40.5 to 665.1 by estimating U_0 with the square root of the granular temperature, and consequently the lubrication force has little effect on the particle–particle drag force. In addition, the lubrication force has an impact on the microstructure of suspensions and therefore indirectly influences the particle–particle drag force. For the low-Stokes-number suspensions, it takes a long time for the particle pairs close to each other to overcome the lubrication force and separate, which leads to an enormous value of the radial distribution function at contact. In the current range of Stokes number, the particle inertia allows a particle pair to approach and separate with a negligible effect of the lubrication force, and as a result the microstructure of the suspensions approaches that of hard-sphere fluids (Koch & Hill 2001). We should also note that the system size of the suspensions is sufficiently small to ensure that the homogeneous state of the suspensions is stable (Koch & Sangani 1999; Garzo 2015; Fullmer & Hrenya 2017).

The paper is structured as follows. In § 2, a brief review of the derivation of the momentum equation and the particle–particle drag relation is given. In § 3, the simulation method is explained in detail. In § 4, the particle–particle drag relation of Zhao & Wang (2021) is validated against simulation results, and a new methodology is proposed. In § 5, MFM simulations are performed to verify the proposed model. In the last section, the important aspects of the present work are summarized.

2. Derivation of the momentum equation and the particle–particle drag relation

For completeness, a brief review of the derivation of the momentum equation for a particular particle type is shown as follows, and readers can refer to Garzo, Dufty & Hrenya (2007), Marchisio & Fox (2013) and Zhao & Wang (2021) for more details. The single-particle VDF of particle type i is denoted by $f_i(c_i, \mathbf{r}, t)$, and $f_i(c_i, \mathbf{r}, t) dc_i d\mathbf{r}$ is equivalent to the probable number of particles in the velocity and position element

$dc_i dr$ at time t . Similarly, the two-particle VDF is represented by $f_{ij}^{(2)}(c_i, r_i, c_j, r_j, t)$, and $f_{ij}^{(2)}(c_i, r_i, c_j, r_j, t) dc_i dr_i dc_j dr_j$ equals the probable number of the particle pairs in which the two particles are respectively lying in velocity and position elements $dc_i dr_i$ and $dc_j dr_j$. The spatio-temporal evolution of the single-particle VDF is described by the Boltzmann equation

$$\frac{\partial f_i}{\partial t} + c_i \cdot \nabla_r f_i + \nabla_{c_i} \cdot (a_i f_i) = \frac{\partial_e f_i}{\partial t}, \tag{2.1}$$

where ∇_r and ∇_{c_i} are the gradient with respect to the position r and the divergence with respect to the velocity c_i , respectively, and a_i is the acceleration of a particle of type i due to the external force, such as the gas-particle drag force. The term on the right-hand side represents the rate at which the single-particle VDF is changed by collisions and has the following form:

$$\frac{\partial_e f_i}{\partial t} = \sum_j \iint_{g \cdot k > 0} \left[\frac{1}{e_{ij}^2} f_{ij}^{(2)}(c_i^b, r, c_j^b, r - d_{ij}k, t) - f_{ij}^{(2)}(c_i, r, c_j, r + d_{ij}k, t) \right] d_{ij}^2 (g \cdot k) dk dc_j. \tag{2.2}$$

Here, e_{ij} is the coefficient of restitution, d_{ij} is the arithmetic mean diameter, k is the unit vector directed from the centre of a particle of type i to the centre of a particle of type j and $g = c_i - c_j$. The superscript b denotes the property before the inverse collision, and the prime will be used to indicate the property after the direct collision. The inverse collision is defined as collisions after which the pre-collision velocities (c_i^b, c_j^b) are changed into (c_i, c_j) , and the direct collision is defined as collisions after which the pre-collision velocities (c_i, c_j) are changed into (c'_i, c'_j) .

Let ψ_i be any particle property. In general, ψ_i is a function of c_i and invariable with r and t . The mean value of ψ_i , i.e. the hydrodynamic property of particle type i , is defined by

$$n_i \langle \psi_i \rangle = \int \psi_i f_i dc_i, \tag{2.3}$$

where n_i is the particle number density. Multiplying ψ_i and integrating over c_i on both sides of (2.1) yields the transport equation of particle type i

$$\frac{\partial n_i \langle \psi_i \rangle}{\partial t} + \nabla_r \cdot (n_i \langle \psi_i c_i \rangle) - n_i \langle a_i \cdot \nabla_{c_i} \psi_i \rangle = \Psi_i(\psi_i). \tag{2.4}$$

Using Taylor expansion and neglecting the second-order and higher-order terms, the collision source term Ψ_i can be decomposed into a collision source term Φ_i and a collision flux term Ω_i as follows:

$$\Psi_i(\psi_i) = \Phi_i(\psi_i) - \nabla_r \cdot \Omega_i(\psi_i), \tag{2.5}$$

where

$$\Phi_i(\psi_i) = \sum_j d_{ij}^2 \iiint_{g \cdot k > 0} (\psi'_i - \psi_i) \chi_{ij} \left(f_i f_j - \frac{d_{ij}}{2} k \cdot f_i f_j \nabla_r \ln \frac{f_i}{f_j} \right) (g \cdot k) dk dc_j dc_i, \tag{2.6}$$

$$\Omega_i(\psi_i) = \sum_j \frac{d_{ij}^3}{2} \iiint_{g \cdot k > 0} (\psi'_i - \psi_i) \chi_{ij} \left(-f_i f_j + \frac{d_{ij}}{2} k \cdot f_i f_j \nabla_r \ln \frac{f_i}{f_j} \right) k (g \cdot k) dk dc_j dc_i. \tag{2.7}$$

In the above equations, the correlation of the pre-collision velocities is neglected, i.e. the assumption of molecular chaos, and therefore the two-particle VDF can be written as the product of the two single-particle VDFs with the pair correlation function χ_{ij} . For inertial particles, the assumption of molecular chaos is valid when the total solid volume fraction is very small ($\phi \ll 0.1$). The reason for this is twofold. First, the collision interval is long enough so that post-collision velocities can relax completely. Second, the particle motion is less restricted, leading to a low probability of repeated collisions. Both of these two aspects weaken the correlation between pre-collision velocities. However, for dense systems, the assumption of molecular chaos may be invalid (Chapman & Cowling 1970). When $\psi_i = m_i c_i$ where m_i is the particle mass, the momentum equation for particle type i is obtained from (2.4) and (2.5) and reads

$$\frac{\partial \phi_i \rho_i \mathbf{u}_i}{\partial t} + \nabla_r \cdot (\phi_i \rho_i \mathbf{u}_i \mathbf{u}_i) = -\nabla_r \cdot \mathbf{p}_i + \phi_i \rho_i \langle \mathbf{a}_i \rangle + \Phi_i(m_i c_i). \quad (2.8)$$

Here, $\mathbf{u}_i = \langle c_i \rangle$, and $\phi_i \rho_i = n_i m_i$, where ϕ_i and ρ_i are respectively the particle volume fraction and the particle mass density. The stress tensor $\mathbf{p}_i = \phi_i \rho_i \langle C_i C_i \rangle + \Omega_i(m_i c_i)$ in which the peculiar velocity $C_i = c_i - \mathbf{u}_i$. $\Phi_i(m_i c_i)$ is the particle–particle drag force experienced by particle type i per unit volume and is the focus of the present study.

In a collision, the relation between the pre-collision velocity c_i and post-collision velocity c'_i is

$$c'_i = c_i - \frac{m_j}{m_i + m_j} (1 + e_{ij}) (\mathbf{g} \cdot \mathbf{k}) \mathbf{k}. \quad (2.9)$$

The present study considers the particle–particle drag force at first approximation, so the gradient terms in (2.6) and (2.7) are neglected. Substituting equation (2.9) into the equation of $\Phi_i(m_i c_i)$, the integral form of the particle–particle drag force is finally given by

$$\Phi_i(m_i c_i) = - \sum_j d_{ij}^2 \frac{m_i m_j}{m_i + m_j} (1 + e_{ij}) \iiint_{\mathbf{g} \cdot \mathbf{k} > 0} \chi_{ij} f_i f_j (\mathbf{g} \cdot \mathbf{k})^2 \mathbf{k} \, d\mathbf{k} \, dc_j \, dc_i. \quad (2.10)$$

It should be noted that, due to symmetry, Φ_i is zero when $i = j$, which means that only collisions between different particle types contribute to the particle–particle drag force. At the first approximation, the single-particle VDF is Maxwellian and reads

$$f_i = \frac{n_i}{(2\pi T_i)^{3/2}} e^{-(c_i - \mathbf{u}_i)^2 / (2T_i)}, \quad (2.11)$$

where T_i is the granular temperature and defined by

$$T_i = \frac{\langle C_i^2 \rangle}{3}. \quad (2.12)$$

Note that the equipartition of the kinetic energy of the peculiar motion indicates $m_i T_i = m_j T_j$. Zhao & Wang (2021) rigorously derived the particle–particle drag relation from (2.10) and (2.11) without any mathematical approximations, and it is given as

$$\begin{aligned} \mathcal{L}_{ij} = & -2\pi d_{ij}^2 \frac{m_i m_j}{m_i + m_j} (1 + e_{ij}) n_i n_j (T_i + T_j) \chi_{ij} \left[\frac{1}{\sqrt{\pi}} \left(\frac{1}{2} + \frac{1}{4\langle g^* \rangle^2} \right) e^{-\langle g^* \rangle^2} \right. \\ & \left. + \left(\frac{\langle g^* \rangle}{2} + \frac{1}{2\langle g^* \rangle} - \frac{1}{8\langle g^* \rangle^3} \right) \text{erf}(\langle g^* \rangle) \right] \langle g^* \rangle, \end{aligned} \quad (2.13)$$

in which $\mathbf{g}^* = \mathbf{g} / \sqrt{2(T_i + T_j)}$ and the error function is defined by $\text{erf}(\langle g^* \rangle) = (2/\sqrt{\pi}) \int_0^{\langle g^* \rangle} e^{-y^2} dy$. Notice that the summation notation is dropped in (2.13) since

bidisperse mixtures are considered in this study, and \mathbf{f}_{ij} represents the particle–particle drag force on the particle type i exerted by j per unit volume. For the latter analysis, the number of collisions per time per unit volume between particle types i and j is denoted by N_{ij} , and N_{ij}/n_i , named the collision frequency, is the average number of collisions experienced by a particle of type i with particle type j . The relation of N_{ij}/n_i proposed by Zhao & Wang (2020) is

$$\frac{N_{ij}}{n_i} = \sqrt{2\pi}d_{ij}^2n_j\sqrt{T_i + T_j}\chi_{ij} \left[e^{-(g^*)^2} + \sqrt{\pi} \left(g^* + \frac{1}{2\langle g^* \rangle} \right) \text{erf}(\langle g^* \rangle) \right]. \quad (2.14)$$

When the particle distribution is homogeneous and isotropic, the pair correlation function only depends on the radial distance and degenerates into the radial distribution function. For the contact value of the radial distribution function, Lebowitz (1964) proposed the following expression for a mixture of hard spheres:

$$\chi_{ij} = \frac{1}{1 - \phi} + \frac{3d_i d_j}{(1 - \phi)^2(d_i + d_j)} \left(\frac{\phi_i}{d_i} + \frac{\phi_j}{d_j} \right), \quad (2.15)$$

where the total solid volume fraction $\phi = \phi_i + \phi_j$. Simulation results show that, in the current parameter range, χ_{ij} is invariant with respect to the Reynolds number, and the prediction error of (2.15) is less than 5%, indicating that the microstructure of the suspensions is close to binary hard-sphere fluids. Therefore, (2.15) is employed in the calculations of the particle–particle drag force and the collision frequency.

3. Simulation method

The second-order accurate immersed boundary-lattice Boltzmann method (IB-LBM) developed by Zhou & Fan (2014) is employed to solve the gas flow, and the particle motion is tracked by the DEM. The particle collision is simulated by the soft-sphere model and resolved by 8 LBM time steps, each containing 15 DEM time steps. The reader can refer to the document of MFIX (Garg *et al.* 2012) for more details. The accuracy of these methods is proved by simulating flow past arrays of rotating spheres (Zhou & Fan 2015a,b) and gas–particle suspensions (Duan *et al.* 2020; Zhao, Chen & Zhou 2021). When the gap size between a pair of particles becomes comparable to the grid size, the flow in the gap is not fully resolved, and consequently the lubrication force cannot be correctly computed. In this situation, a theoretical formula (Guazzelli & Morris 2012) is adopted to compensate for the unresolved part of the lubrication force and is given by

$$\mathbf{F}_{ij}^l = -\frac{3\pi\mu}{2} \left(\frac{d_i d_j}{d_i + d_j} \right)^2 \frac{(\mathbf{g} \cdot \mathbf{k})\mathbf{k}}{|\mathbf{r}_i - \mathbf{r}_j| - d_{ij}}, \quad (3.1)$$

where μ is the dynamic viscosity of the gas. The detailed implementation can be found in Nguyen & Ladd (2002), Simeonov & Calantoni (2012) and Brandle de Motta *et al.* (2013)

Initially, a particle configuration, the microstructure of which is identical to that of a bidisperse hard-sphere fluid, is generated by the Monte Carlo procedure in a fully periodic cube (Hill, Koch & Ladd 2001), and the particle velocity is set to zero. Then, the gas and particle phases start to move freely under gravity and an upward pressure gradient. Since the particle density is larger than the gas, the particle phase accelerates downward relative to the gas phase, and therefore the slip velocity between the gas and particle phases increases. The increase rate of the slip velocity decreases because the gas–particle drag force increases with the slip velocity. Finally, the increase rate of the

slip velocity is close to zero, and the slip velocity is statistically stationary. The value of the gravitational acceleration is varied so that different particle Reynolds numbers are obtained. The reported particle Reynolds number is computed after the flow reaches its statistically steady state. The pressure gradient is dynamically adjusted in simulations to keep the total volumetric flux of the flow constant (Fullmer *et al.* 2017). The flow simulated in this study corresponds to sedimentation or fluidization in a fully periodic domain, depending on whether the constant is zero or not. Note that the physics should not change with the constant. The quantities of interest are first averaged over a period of simulation time after the statistically stationary state is reached and then averaged over three different initial particle configurations. For instance, the mean particle–particle drag force is computed as follows:

$$\bar{f}_{ij} = \frac{\sum_{s=1}^3 \sum_{k=1}^N \sum_{m=1}^{N_i} \sum_{n=1}^{N_j} F_{im,jn}^c(t_k, s)}{3NV}, \quad (3.2)$$

where $F_{im,jn}^c(t_k, s)$ is the collision force on *no. m* particle of type *i* exerted by *no. n* particle of type *j* at time t_k for the initial particle configuration *s*, where *N* is the number of time slices, N_i and N_j are, respectively, the particle numbers of type *i* and *j* and *V* is the volume of the computation domain. As was always done for the gas–particle drag force, \bar{f}_{ij} is normalized by the Stokes drag force as follows:

$$F_{ij}^c = \frac{\bar{f}_{ij} \cdot U_i}{3\pi\mu d_i U_i^2 n_i}, \quad (3.3)$$

in which U_i is the superficial gas velocity relative to particle type *i*, and equals $(1 - \phi)(\mathbf{u}_g - \mathbf{u}_i)$. Here, \mathbf{u}_g is the gas velocity. It is found from simulation results that the ratio of the particle–particle drag force to the gas–particle drag force is 0.16 (maximum 0.20), 0.31 (maximum 0.36) and 0.37 (maximum 0.42) for $d_l/d_s = 1.2, 1.6$ and 2 , respectively, which indicates that the particle–particle drag force cannot be neglected in predicting the segregation phenomenon.

The ratio of the particle mass density to the gas density is fixed at 1000, ensuring that the effect of the lubrication force on the particle collision is quite small in the current range of the Reynolds number. In order to keep the suspensions homogeneous and save computational costs, the edge length of the computation domain is chosen to be five times the diameter of large particles. The effect of the domain size on the particle–particle drag force is studied in Appendix A. The particle collision is assumed elastic and frictionless. The ranges of other parameters are listed in table 1. In LBM simulations, the quantities are in lattice units, and the conversion between lattice units and physical units can be readily achieved by exploiting the fact that key dimensionless numbers are the same between different systems of units. According to the law of similarity, the physics obtained from a case applies to the cases with the same geometry and key dimensionless numbers, regardless of what the values of physical quantities are. Therefore, only the critical geometry parameters and key dimensionless numbers are provided in table 1.

It has been found that the relative velocity $\langle g \rangle$, the granular temperature $T_s(T_l)$ and the particle–particle drag force \bar{f}_{sl} are less sensitive to the grid resolution. Here, the subscripts *s* and *l* respectively denote small and large particles. For the case of $\phi = 0.3$ and $\langle Re_p \rangle \approx 113.5$, relative to the results at the grid resolution of $d_s/20$, the deviations of $\langle g \rangle$, $T_s(T_l)$ and \bar{f}_{sl} at the grid resolution of $d_s/12$ are 5.7 %, 0.2 % (1.1 %) and 0.6 %, respectively, and the

ϕ	0.1, 0.2, 0.3
x_s	0.1, 0.3, 0.5
d_l/d_s	1.2, 1.6, 2
$\langle Re_p \rangle$	6.7 ~ 123.8
St_{hs}/St_{hl}	42.9 ~ 729.1/44.5 ~ 895.5
St_{cs}/St_{cl}	7.5 ~ 98.5/13.5 ~ 330.1

Table 1. The parameter ranges in the present study. The subscripts s and l respectively denote small and large particles. Here, ϕ is the total solid volume fraction, and x_s is the ratio of the solid volume fraction of small particles to the total solid volume fraction, that is, $x_s = \phi_s/\phi$; $\langle Re_p \rangle$ represents the mean particle Reynolds number defined based on the Sauter mean diameter $\langle d \rangle_{32}$ and the mean of the superficial relative velocity $\langle U \rangle$; $\langle d \rangle_{32} = 1/(\sum_i x_i/d_i)$ and $\langle U \rangle = \sum_i x_i U_i$; St_{hi} is the hydrodynamic Stokes number with the expression of $d_i \rho_i U_i / (18\mu F_{di})$, where F_{di} is the gas–particle drag force normalized by the Stokes drag force, i.e. $3\pi\mu d_i U_i$; St_{hi} is the ratio of the particle inertial response time to the flow time scale; St_{ci} is the collision Stokes number with the expression of $d_i^2 \rho_i \sum_j N_{ij} / (18\mu F_{di} n_i)$, representing the ratio of the particle inertial response time to the inter-collision time. When $d_l/d_s = 1.2$ or 1.6, only the cases of $x_s = 0.3$ are simulated.

deviations at the grid resolution of $d_s/16$ are 0.8 %, 0.5 % (1.1 %) and 0.6 %, respectively. In this study, the grid size of $d_s/16$ is adopted.

4. Application of the particle–particle drag relation to bidisperse gas–particle suspensions

Figures 1(a) and 1(b) respectively show the collision frequency between small and large particles and the particle–particle drag force of small particles at various $\langle Re_p \rangle$ and ϕ . The volume fraction of small particles x_s is around 0.3, and the particle diameter ratio is 2. For other cases listed in table 1, that is, $x_s = 0.1$, $x_s = 0.5$, $d_l/d_s = 1.2$ and $d_l/d_s = 1.6$, similar behaviour is found and therefore they are not shown for brevity. As the particle Reynolds number increases, the granular temperature increases. Consequently, the collision frequency and the particle–particle drag force increase. The predictions of the collision frequency by (2.14) agree well with the simulation results. However, (2.13) seriously overestimates the particle–particle drag force, especially when the total solid volume fraction is high, and its deviations at $\phi = 0.1, 0.2$ and 0.3 are 34 %, 68 % and 89 %, respectively.

For the cases in figure 1, the mean of the skewness and the mean of the kurtosis (the kurtosis of the normal distribution, i.e. 3, is subtracted) of the single-particle VDFs are both smaller than 0.1, indicating the assumption of the Maxwellian is valid. The ratio of the granular temperature in the streamwise direction to the non-streamwise direction is 1.15 on average. However, there is no apparent correlation between the ratio and the total solid volume fraction, which is inconsistent with the tendency of in the deviations of (2.13) shown in figure 1(b), and hence the slight anisotropy is not the cause of the poor performance of (2.13). Before further analysis, the mean free path of particle type i , in the reference frame of the mass centre of particle type j , will first be derived. The mean free path is the mean distance travelled by a particle between successive collisions during a given time and is defined by

$$l_i = \frac{n_i \langle v_i \rangle \Delta t}{n_i \Delta t / \tau_i}, \tag{4.1}$$

where τ_i is the collision interval and equals to $n_i / (N_{ii} + N_{ij})$. In the reference frame of the mass centre of particle type j , the velocity of a particle of type i , denoted by \mathbf{v}_i , is $\mathbf{c}_i - \mathbf{u}_j$, and the mean of \mathbf{v}_i is the relative velocity $\langle \mathbf{g} \rangle$. The mean of the module of \mathbf{v}_i is

Particle–particle drag force

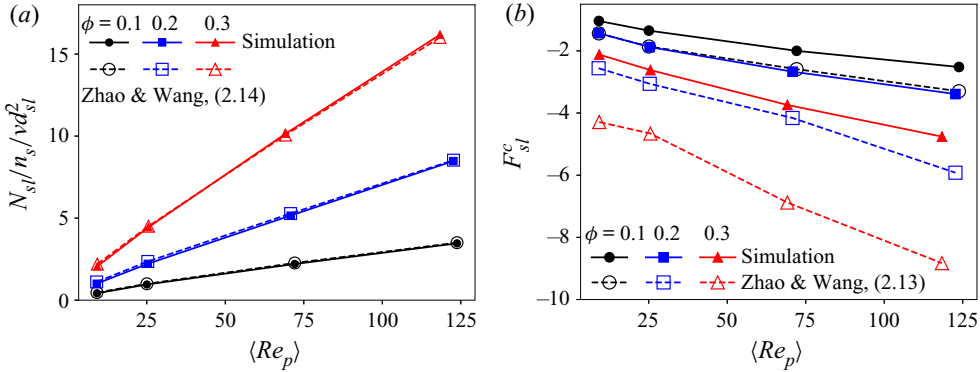


Figure 1. Simulated and predicted values of (a) the collision frequency between small particles and large particles and (b) the particle–particle drag force of small particles exerted by large particles at various $\langle Re_p \rangle$ and ϕ . The collision frequency is normalized by v/d_{sl}^2 , where v is the kinematic viscosity of the gas and the particle–particle drag force is normalized by the Stokes drag force. The volume fraction of small particles x_s is around 0.3, and the particle diameter ratio is 2. The circle, square and triangle symbols respectively correspond to $\phi = 0.1, 0.2$ and 0.3 . Solid and void symbols respectively denote the simulation results and the predictions by the equations of Zhao & Wang (2020, 2021), i.e. (2.14) in (a) and (2.13) in (b).

then computed from (2.3) and (2.11) with c_i and u_i replaced by v_i and $\langle g \rangle$ respectively. By the integral method in Glansdorff (1962), Zhao & Wang (2020), the final form of $\langle v_i \rangle$ is

$$\langle v_i \rangle = \sqrt{\frac{2T_i}{\pi}} e^{-\langle g \rangle^2/(2T_i)} + \left(\langle g \rangle + \frac{T_i}{\langle g \rangle} \right) \operatorname{erf} \left(\frac{\langle g \rangle}{\sqrt{2T_i}} \right). \quad (4.2)$$

We should note that, when $\langle g \rangle = 0$, the above equation reduces to the form $\langle v_i \rangle = 2\sqrt{2T_i/\pi}$, which is the relation of $\langle C_i \rangle$ proposed in the book of Chapman & Cowling (1970).

Figure 2 shows the collisions between a small particle, labelled by m , and large particles during $20\tau_{sl}$. Here, τ_{sl} is the mean of the collision interval between small particles and large particles and equals n_s/N_{sl} . Once a small particle collides with a large particle, over the following time, the small particle will probably be trapped within the space around the large particle, and bounce back and forth, with a much shorter interval than τ_{sl} , among the large particle and its neighbours. For example, during the time period $t/\tau_{sl} = 14.8 \sim 18.8$, the small particle m is trapped within the space between the large particles of no. 13 and no. 21, and in turn collides with them by an interval of $0.44\tau_{sl}$. Note that other small particles also play a role in trapping the small particle m . Similar phenomena can also be found in the time periods $t/\tau_{sl} = 0.1 \sim 1.6$ ($0.21\tau_{sl}$) and $8.7 \sim 11.7$ ($0.43\tau_{sl}$), and these time periods are named the time period of trapping for brevity (indicated by the shadows in figure 2). Under the prerequisite condition of $\tau_{sl} < \tau_{ps}$, a shorter collision interval gives a smaller relative velocity. This is because the collisions between different particle types reduce their relative velocity. Here, τ_{ps} is the small-particle relaxation time and can be roughly estimated by $d_s^2\rho_s/(18\mu F_{ds})$ (Zaichik *et al.* 2009). It can be calculated by simulation results that $\tau_{ps}/\tau_{sl} \sim O(10)$ in this case. Consequently, it is expected that the relative velocity over the time period of trapping is statistically smaller than the relative velocity over the entire time period. Because most of the collision events occur during the time period of trapping, it is more reasonable to use the relative velocity over this time period instead of that over the entire time period. By fitting (2.13) and (2.14) with polynomials, it has been found that for $\langle g^* \rangle < 1$ in this study, N_{ij} is insensitive to $\langle g^* \rangle$ and

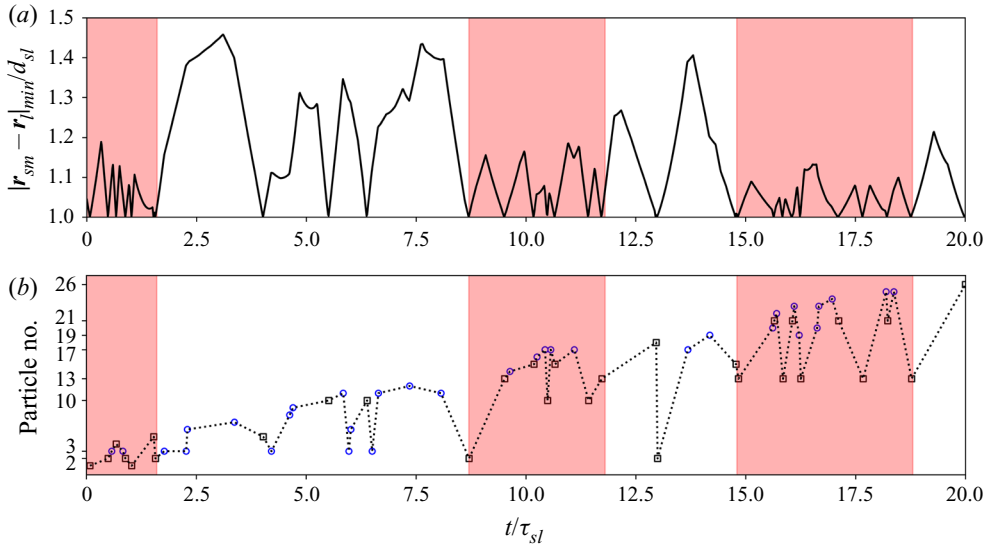


Figure 2. The collisions between a small particle, labelled by the subscript m , and large particles during $20\tau_{sl}$ for the case of $\phi = 0.3$, $x_s \approx 0.3$, $d_l/d_s = 2$ and $\langle Re_p \rangle \approx 69.2$. The shadows indicate the time periods of trapping. (a) The instantaneous change of the minimum distance between the small particle m and large particles, normalized by the arithmetic mean diameter d_{sl} . Here, $|r_{sm} - r_l|_{min}/d_{sl} = 1$ implies the collision between the small particle m and a large particle. (b) Number of the particles that collided with the small particle m . Circles and squares respectively denote small and large particles. According to the time sequence of collisions, the shown particles are labelled by no. 1, 2, 3, ...

f_{ij} almost linearly increases as $\langle g^* \rangle$. Therefore, with the mean of the relative velocity over the entire time period, (2.14) well predicts the collision frequency, but (2.13) significantly overestimates the particle–particle drag force. Considering that the small particle that has just collided with a large particle will collide with other particles on average at the location l_s away from the large particle, and then be probably bounced back and trapped, in what follows, the relative velocity during the time period when the relative distance of the particle pair is smaller than a mean free path l_s is assumed to be relevant to the particle–particle drag force.

The position and velocity of each particle in a computational domain are collected after a statistically stationary state has been reached, and then the relative velocity of each particle pair of different size, $\mathbf{g} = \mathbf{c}_s - \mathbf{c}_l$, is binned in terms of the distance $|\mathbf{r}_s - \mathbf{r}_l|$ and θ_k , which is the angle between \mathbf{k} and the flow direction. Recall that \mathbf{k} is the unit vector along $\mathbf{r}_l - \mathbf{r}_s$. Figure 3 shows the geometry of the left part of a bin in two dimensions, denoted by ΔA , and the geometry in three dimensions is obtained by rotating ΔA around the z -axis. Figure 4 is the contour plot of the mean of the relative velocities within each bin, $\langle \mathbf{g} \rangle(\theta_k, |\mathbf{r}_s - \mathbf{r}_l|)$, normalized by that within the entire domain, $\langle \mathbf{g} \rangle$. Because the distribution of the relative velocity is symmetrical about the z -axis of the spherical coordinate system $(\theta_k, |\mathbf{r}_s - \mathbf{r}_l|, \varphi)$ shown in figure 3, the x and y components of $\langle \mathbf{g} \rangle(\theta_k, |\mathbf{r}_s - \mathbf{r}_l|)$ and $\langle \mathbf{g} \rangle$ are close to zero. As discussed earlier, a small particle is easily trapped within the space around a large particle, and statistically has a velocity close to that of the large particle. As a result, the regions of the low relative velocity are formed near large particles, as shown in figure 4. As the total solid volume fraction increases, the distance that the trapped small particle is allowed to travel becomes smaller and smaller, and therefore the regions of low relative velocity gradually shrink. In the

Particle–particle drag force

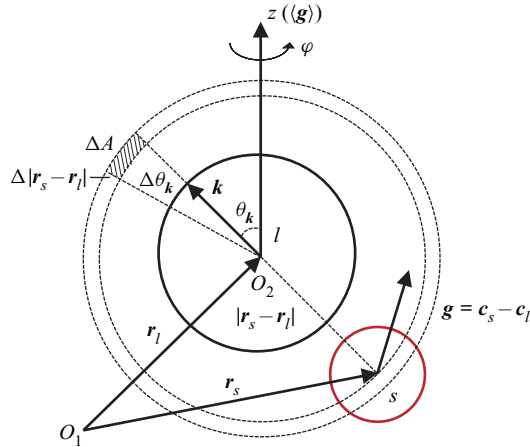


Figure 3. Geometry of the left part of a bin in two dimensions, which is denoted by ΔA and indicated by the shadowed area. Here, O_1 is the origin of a fixed coordinate system, and O_2 is the origin of a spherical coordinate system $(\theta_k, |r_s - r_l|, \phi)$, co-moving with large particles. The z -axis of the spherical coordinate system coincides with the flow direction. The geometry of a bin in three dimensions is obtained by rotating ΔA around the z -axis.

streamwise direction, the collision force, which hinders the growth of the relative velocity, decreases with θ_k approaching $\pi/2$, and therefore the relative velocity increases under the action of the gas–particle drag force, as shown in figure 4. The mean free path signified by the dotted line decreases as ϕ increases since the collision frequency increases with ϕ . The modules of the mean relative velocities within the mean free path, denoted by $\langle g \rangle (|r_s - r_l| < l_s)$, respectively equal $0.93\langle g \rangle$, $0.88\langle g \rangle$ and $0.78\langle g \rangle$ when $\phi = 0.1, 0.2$ and 0.3 . With $\langle g \rangle (|r_s - r_l| < l_s)$, the predictions of (2.13) will be smaller and hence become closer to the simulation results. However, before doing that, the effect of the anisotropy observed in figure 4 on the particle–particle drag force is first discussed.

By symmetry, the collision forces cancel each other in the directions perpendicular to the flow direction, and therefore only the streamwise component contributes to the particle–particle drag force. The streamwise component of the collision force varies with the polar angle as the function $\cos \theta_k$, and consequently the relative velocity also changes as a function of θ_k , as mentioned above. It is necessary to consider the correlation between the two functions in calculating the particle–particle drag force. For example, the relative velocity is large around $\theta_k = \pi/2$, but the streamwise component of the collision force in this region is close to zero. Therefore, it can be expected that (2.13) will overestimate the particle–particle drag force by neglecting the anisotropic distribution of the relative velocity. A feasible way to consider the correlation is first to compute the particle–particle drag forces at different polar angles and then sum them up. Assuming the single-particle VDF at each polar angle is Maxwellian, the derivation process of the particle–particle drag force at a specific polar angle is given as follows:

$$\begin{aligned}
 f_{sl} &= -d_{sl}^2 \frac{m_s m_l}{m_s + m_l} (1 + e_{sl}) \chi_{sl} \iiint_{\mathbf{g} \cdot \mathbf{k} > 0} f_s f_l (\mathbf{g} \cdot \mathbf{k})^2 \mathbf{k} \, d\mathbf{k} \, d\mathbf{c}_l \, d\mathbf{c}_s \\
 &= -d_{sl}^2 \frac{m_s m_l}{m_s + m_l} (1 + e_{sl}) \frac{\chi_{sl} n_s n_l}{(2\pi)^3 (T_s T_l)^{3/2}} \iiint_{\mathbf{g} \cdot \mathbf{k} > 0} \\
 &\quad \times e^{-[c_s - u_s(\theta_k)]^2 / (2T_s) - [c_l - u_l(\theta_k)]^2 / (2T_l)} (\mathbf{g} \cdot \mathbf{k})^2 \mathbf{k} \, d\mathbf{k} \, d\mathbf{c}_l \, d\mathbf{c}_s. \quad (4.3)
 \end{aligned}$$

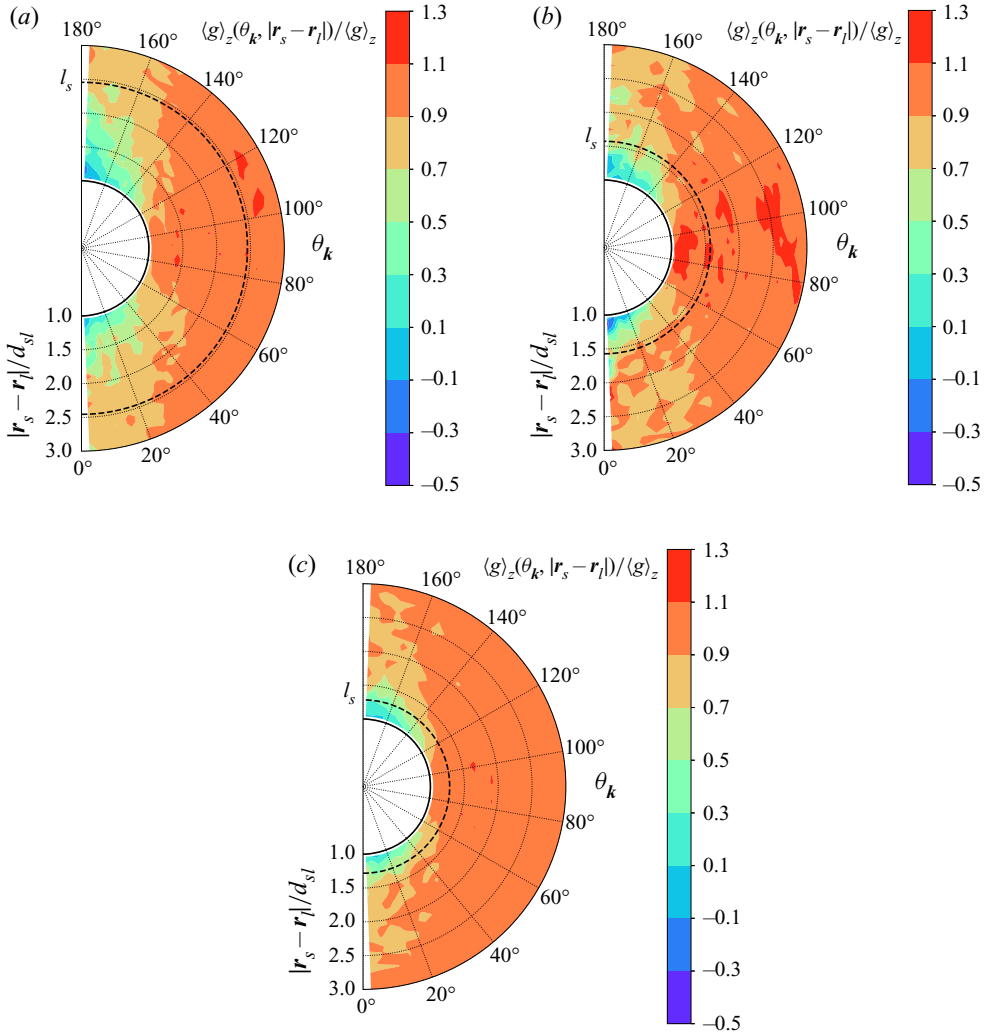


Figure 4. Contour plot of the relative velocity of particle pairs of different size in a polar coordinate system $(\theta_k, |r_s - r_l|)$. The meanings of θ_k and $|r_s - r_l|$ are described in figure 3. The subscript z denotes the streamwise direction. The dotted line indicates $|r_s - r_l| = l_s$, where l_s is the mean free path of small particles and calculated by (4.1) and (4.2). Here, $x_s \approx 0.3$, $d_l/d_s = 2$, $\langle Re_p \rangle \approx 70.7$ and (a) $\phi = 0.1$, (b) $\phi = 0.2$, (c) $\phi = 0.3$.

Note that u_s and u_l vary with θ_k in this equation. By the integral method employed in Glansdorff (1962) and Zhao & Wang (2020), the above equation can be transformed into

$$f_{sl} = C \int e^{-(T_s+T_l)/(2T_sT_l)(G-\langle G \rangle)^2} dG \iint_{\mathbf{g} \cdot \mathbf{k} > 0} e^{-[g-\langle g \rangle(\theta_k)]^2/(2(T_s+T_l))} (\mathbf{g} \cdot \mathbf{k})^2 \mathbf{k} dg d\mathbf{k}, \tag{4.4}$$

where $G = (T_s c_l + T_l c_s)/(T_s + T_l)$, and $dc_l dc_s = dG dg$ according to the Jacobian determinant. Here, C is the constant before the integral sign of (4.3). The integral of \mathbf{g} is carried out in the spherical coordinates where the z -axis coincides with \mathbf{k} and is

given as

$$\begin{aligned} f_{sl} &= C \left(\frac{2\pi T_s T_l}{T_s + T_l} \right)^{3/2} \iint_{\mathbf{g} \cdot \mathbf{k} > 0} e^{-g^2/(2(T_s+T_l))} (\mathbf{g} \cdot \mathbf{k})^2 \mathbf{k} \, d\mathbf{g}' \, d\mathbf{k} \\ &= 2\pi C \left(\frac{2\pi T_s T_l}{T_s + T_l} \right)^{3/2} \int_{\mathbf{g} \cdot \mathbf{k} > 0} e^{-g^2/(2(T_s+T_l))} (g \cos \theta_g)^2 g'^2 \sin \theta_{g'} \, d\theta_{g'} \, d\mathbf{g}' \, d\mathbf{k}. \end{aligned} \quad (4.5)$$

From $\mathbf{g} \cdot \mathbf{k} = [\langle \mathbf{g} \rangle(\theta_k) + \mathbf{g}'] \cdot \mathbf{k}$, i.e. $g \cos \theta_g = \langle g \rangle(\theta_k) \cos \psi_k + g' \cos \theta_{g'}$, we have that $\mathbf{g} \cdot \mathbf{k} > 0$ is equivalent to $\cos \theta_{g'} > -\langle g \rangle(\theta_k) \cos \psi_k / g'$. Here, ψ_k is the angle between $\langle \mathbf{g} \rangle(\theta_k)$ and \mathbf{k} . Let $x = \cos \theta_{g'}$, (4.5) is changed into

$$\begin{aligned} f_{sl} &= 2\pi C \left(\frac{2\pi T_s T_l}{T_s + T_l} \right)^{3/2} \int_D e^{-g^2/(2(T_s+T_l))} [\langle g \rangle(\theta_k)^2 g'^2 \cos^2 \psi_k + g'^4 x^2 \\ &\quad + 2\langle g \rangle(\theta_k) g'^3 \cos \psi_k x] \, dx \, d\mathbf{g}' \, d\mathbf{k}. \end{aligned} \quad (4.6)$$

Here, D is the domain of integration. When $0 < \psi_k < \pi/2$

$$\begin{aligned} D &= \{-1 < x < 1, 0 < g' < \langle g \rangle(\theta_k) \cos \psi_k\} \\ &\cup \left\{ -\frac{\langle g \rangle(\theta_k) \cos \psi_k}{g'} < x < 1, \langle g \rangle(\theta_k) \cos \psi_k < g' < +\infty \right\}. \end{aligned} \quad (4.7)$$

When $\pi/2 < \psi_k < \pi$

$$D = \left\{ -\frac{\langle g \rangle(\theta_k) \cos \psi_k}{g'} < x < 1, -\langle g \rangle(\theta_k) \cos \psi_k < g' < +\infty \right\}. \quad (4.8)$$

Equation (4.6) can be integrated by parts, and it is found that the results in both situations, i.e. $0 < \psi_k < \pi/2$ and $\pi/2 < \psi_k < \pi$, are the same

$$\begin{aligned} f_{sl} &= -2\pi d_{sl}^2 \frac{m_s m_l}{m_s + m_l} (1 + e_{sl}) n_s n_l (T_s + T_l) \chi_{sl} \int \left\{ \frac{1}{\sqrt{\pi}} \cos^2 \theta_k e^{-[\langle g^* \rangle(\theta_k) \cos \theta_k]^2} \right. \\ &\quad + \left[\frac{\cos \theta_k}{2\langle g^* \rangle(\theta_k)} + \langle g^* \rangle(\theta_k) \cos^3 \theta_k \right] \operatorname{erf}[\langle g^* \rangle(\theta_k) \cos \theta_k] \\ &\quad \left. + \frac{A \cos \theta_k}{2\langle g^* \rangle(\theta_k)} + A \langle g^* \rangle(\theta_k) \cos^3 \theta_k \right\} \sin \theta_k \langle g^* \rangle(\theta_k) \, d\theta_k, \end{aligned} \quad (4.9)$$

where the integrand function multiplied by $d\theta_k$ is the particle–particle drag force at θ_k . In the above equation, $\cos \psi_k$ is replaced by $\cos \psi_k = A \cos \theta_k$ since $\langle \mathbf{g} \rangle(\theta_k)$ is parallel with $\langle \mathbf{g} \rangle$. Here, $A = 1$ when $\langle \mathbf{g} \rangle(\theta_k)$ is in the direction of $\langle \mathbf{g} \rangle$, and $A = -1$ when $\langle \mathbf{g} \rangle(\theta_k)$ is in the opposite direction of $\langle \mathbf{g} \rangle$.

To compute the particle–particle drag force, the integral in (4.9) is discretized numerically, and the mean of the relative velocity in each discrete interval $\Delta\theta_k$ within the range $|\mathbf{r}_s - \mathbf{r}_l| < l_s$, represented by $\langle \mathbf{g} \rangle(\theta_k, |\mathbf{r}_s - \mathbf{r}_l| < l_s)$, is substituted into the discrete equation. Figure 5 shows the comparison between predictions and simulation results for all simulation cases in this study. The square points are computed by substituting the mean of the relative velocity within the range $|\mathbf{r}_s - \mathbf{r}_l| < l_s$, i.e. $\langle \mathbf{g} \rangle(|\mathbf{r}_s - \mathbf{r}_l| < l_s)$, into (2.13), and therefore do not include the effect of the anisotropy. The predictions by (4.9) are the most accurate with a mean error of 8% (maximum 25%), and the prediction

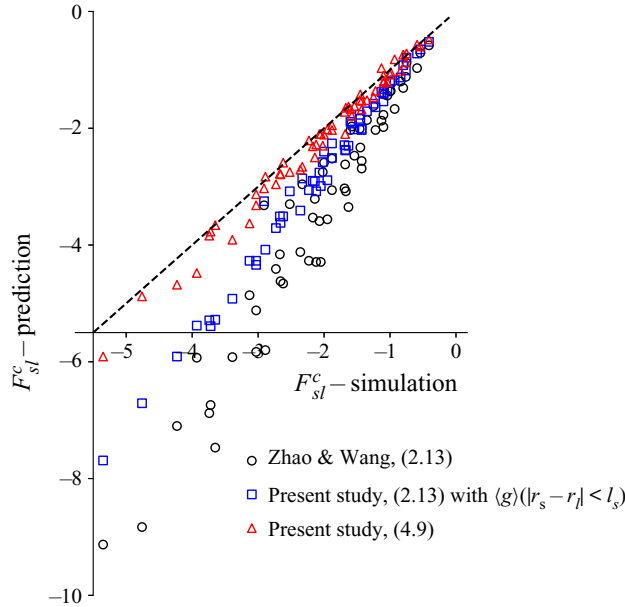


Figure 5. Predictions versus simulation results for the particle–particle drag force of small particles. Circles, squares and triangles respectively represent the predictions calculated by (2.13) with $\langle \mathbf{g} \rangle$, (2.13) with $\langle \mathbf{g} \rangle (|r_s - r_l| < l_s)$ and (4.9) with $\langle \mathbf{g} \rangle (\theta_k, |r_s - r_l| < l_s)$. The dotted line is the bisector line $y = x$. The parameter range is shown in table 1.

by (2.13) with $\langle \mathbf{g} \rangle$ is the worst with a mean error of 61 % (maximum 109 %). The predictions by (2.13) with $\langle \mathbf{g} \rangle (|r_s - r_l| < l_s)$ are between the predictions by (2.13) and (4.9) with a mean error of 32 % (maximum 48 %), which indicates that the anisotropy of the relative-velocity distribution cannot be neglected. Note that (4.9) still slightly overestimates the particle–particle drag force. This may be caused by hydrodynamic interactions between particle pairs.

To apply (4.9) in MFM simulations, the relative velocity within a mean free path of small particles l_s , i.e. $\langle \mathbf{g} \rangle (\theta_k, |r_s - r_l| < l_s)$, must be adequately resolved, which implies that the grid size should be much smaller than l_s . For the case shown in figure 4(c), the mean free path is only $1.28d_{sl}$, leading to a grid size of a small fraction of a large-particle diameter. It is infeasible to use such a fine grid in MFM simulations mainly due to the huge computational cost. With this in mind, the relative velocity $\langle \mathbf{g} \rangle$ in (2.13) is replaced by an effective relative velocity, denoted as $\alpha \langle \mathbf{g} \rangle$, in order to make the predictions of (2.13) agree with those of (4.9), that is

$$f_{sl}(\alpha \langle \mathbf{g} \rangle) = f_{sl}[\langle \mathbf{g} \rangle (\theta_k, |r_s - r_l| < l_s)]. \quad (4.10)$$

The factor α is solved by iteration. With ϕ increasing, the probability of repeated collisions increases since the particle motion is more restricted. Consequently, the correlation between pre-collision velocities becomes stronger, and accordingly, the factor α decreases, as seen in figure 6. The effect of x_s on α is twofold. First, the effect of x_s is the same as the effect of ϕ because the total particle number density increases with x_s . Second, as x_s increases, the collisions between small particles become more frequent, and small particles relax more quickly. This is because the collisions between like particles help a post-collision pair to recover their statistically stationary velocities. If the correlation between pre-collision velocities is mainly controlled by the relaxation process of small

Particle–particle drag force

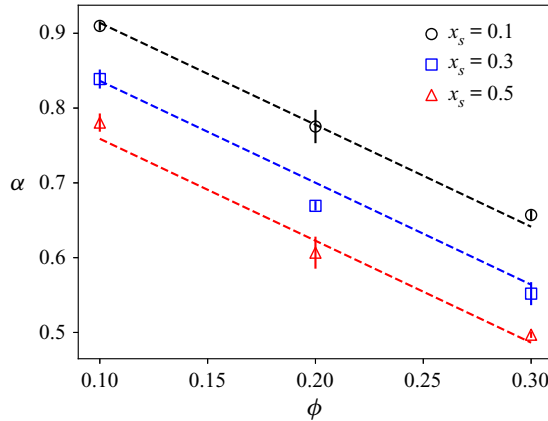


Figure 6. Variation of the factor α , defined by (4.10), with the total solid volume fraction ϕ at different volume fractions of small particles x_s . The error bar characterizes the standard deviation derived from the cases of different particle diameter ratios and particle Reynolds numbers. The dotted lines are the fitting curves given by (4.11).

particles, the correlation becomes weaker and therefore α increases. As shown in figure 6, the factor α decreases with x_s , which indicates the first effect dominates the correlation between pre-collision velocities. Note that the particle diameter ratio and the Reynolds number have a minor effect on α . The factor α is approximately fitted by a linear function of ϕ and x_s , which is given as

$$\alpha = -1.363\phi - 0.3875x_s + 1.089. \quad (4.11)$$

The predictions of (2.13) with $\alpha(\mathbf{g})$ where α is computed by (4.11) are close to that of (4.9), and deviate from simulation results by 10 % on average (23 % maximum).

5. Model assessment

In order to assess the performance of the model proposed in this study, we implement the model

$$\begin{aligned} \mathcal{f}_{ij} = & -2\pi d_{ij}^2 \frac{m_i m_j}{m_i + m_j} (1 + e_{ij}) n_i n_j (T_i + T_j) \chi_{ij} \left[\frac{1}{\sqrt{\pi}} \left(\frac{1}{2} + \frac{1}{4\alpha^2 \langle g^* \rangle^2} \right) e^{-\alpha^2 \langle g^* \rangle^2} \right. \\ & \left. + \left(\frac{\alpha \langle g^* \rangle}{2} + \frac{1}{2\alpha \langle g^* \rangle} - \frac{1}{8\alpha^3 \langle g^* \rangle^3} \right) \text{erf}(\alpha \langle g^* \rangle) \right] \alpha \langle g^* \rangle \\ \alpha = & -1.363\phi - 0.3875x_s + 1.089, \end{aligned} \quad (5.1)$$

in MFIX-MFM and perform MFM simulations. The cases of $\phi = 0.1 \sim 0.3$, $x_s \approx 0.3$, $d_l/d_s = 2$ and $\langle Re_p \rangle \approx 70.7$ are chosen. For comparison, the input parameter settings and boundary conditions are consistent with the PR-DNSs. Assuming the gas is air and the gravitational acceleration equals 9.81 m s^{-2} , the input parameters in lattice units are converted into those in physical units and listed in table 2. The gas–particle drag force is calculated by the model of Beetstra *et al.* (2007), which is appropriate for bidisperse suspensions that are inertial and homogeneous. Benyahia (2008) compared the predictions of several kinetic theories with molecular dynamic data and found the kinetic theory of Iddir & Arastoopour (2005) is the most accurate one. Consequently, the kinetic theory of Iddir & Arastoopour (2005) is adopted in the present study. The grid size of $2.5d_l$ is

ϕ	0.1, 0.2, 0.3
x_s	0.3
d_s	388 μm , 467 μm , 564 μm
d_l	776 μm , 933 μm , 1129 μm
L	3.84 mm, 4.65 mm, 5.64 mm
ρ_f	1.29 kg m^{-3}
ρ_p	1290 kg m^{-3}
μ	19.1×10^{-6} Pa s
g	9.81 m s^{-2}
Δp	4.90 Pa, 11.8 Pa, 21.5 Pa
e	1
C_f	0
t	2s

Table 2. The input parameter settings for MFM simulations. Here, g is the gravitational acceleration, and Δp is the pressure drop across the entire domain, which is used to drive the flow; e and C_f represent the coefficient of restitution and the friction coefficient, respectively; t is the total simulation time.

chosen, and it has been found that the domain-averaged quantities do not change as the grid size decreases to $0.5d_l$.

Besides the model of this study and Zhao & Wang (2021), the models of Syamlal (1987) and Iddir & Arastoopour (2005) are also tested. Note that when $\alpha = 1$, (5.1) degenerates to the model of Zhao & Wang (2021), i.e. (2.13). The models of Syamlal (1987) and Iddir & Arastoopour (2005) are respectively given as

$$\mathbf{f}_{ij} = -d_{ij}^2 \frac{m_i m_j}{m_i + m_j} (1 + e_{ij}) n_i n_j \chi_{ij} \left(\frac{\pi}{2} + \frac{\pi^2 C_f}{8} \right) \langle g \rangle \langle \mathbf{g} \rangle, \quad (5.2)$$

$$\mathbf{f}_{ij} = -\frac{\sqrt{\pi} d_{ij}^2}{4} \frac{m_i m_j}{m_i + m_j} (1 + e_{ij}) n_i n_j \chi_{ij} \left(\frac{1}{T_i T_j} \right)^{3/2} R_2 \langle \mathbf{g} \rangle, \quad (5.3)$$

$$R_2 = \frac{1}{2A_{ij}^{3/2} D_{ij}^2} + \frac{3B_{ij}^2}{A_{ij}^{5/2} D_{ij}^3} + \frac{15B_{ij}^4}{A_{ij}^{7/2} D_{ij}^4} + \dots, \quad (5.4)$$

$$A_{ij} = \frac{T_i + T_j}{2T_i T_j}, \quad B_{ij} = \frac{m_j T_j - m_i T_i}{2(m_i + m_j) T_i T_j}, \quad D_{ij} = \frac{m_i^2 T_i + m_j^2 T_j}{2(m_i + m_j)^2 T_i T_j}. \quad (5.5a-c)$$

In (5.2), the model of Syamlal (1987), C_f denotes the friction coefficient and equals zero in the present study. And in (5.3), the model of Iddir & Arastoopour (2005), the terms including the gradients of the particle number density and granular temperature are neglected because the studied suspensions are homogeneous. In addition, the granular temperature in the paper of Iddir & Arastoopour (2005) includes the particle mass, while the granular temperature in this paper, i.e. T_i , does not.

Figures 7(a), 7(b) and 7(c) respectively plot the dimensionless relative velocity, the particle–particle drag force and the gas–particle drag force as functions of ϕ . For convenience, the abbreviations ZW, IA and S are introduced to respectively represent the models of Zhao & Wang (2021), Iddir & Arastoopour (2005) and Syamlal (1987). As shown in figure 7(a,b), model S highly underestimates the particle–particle drag force due to neglecting the granular temperature. Consequently, the relative velocity predicted

Particle–particle drag force

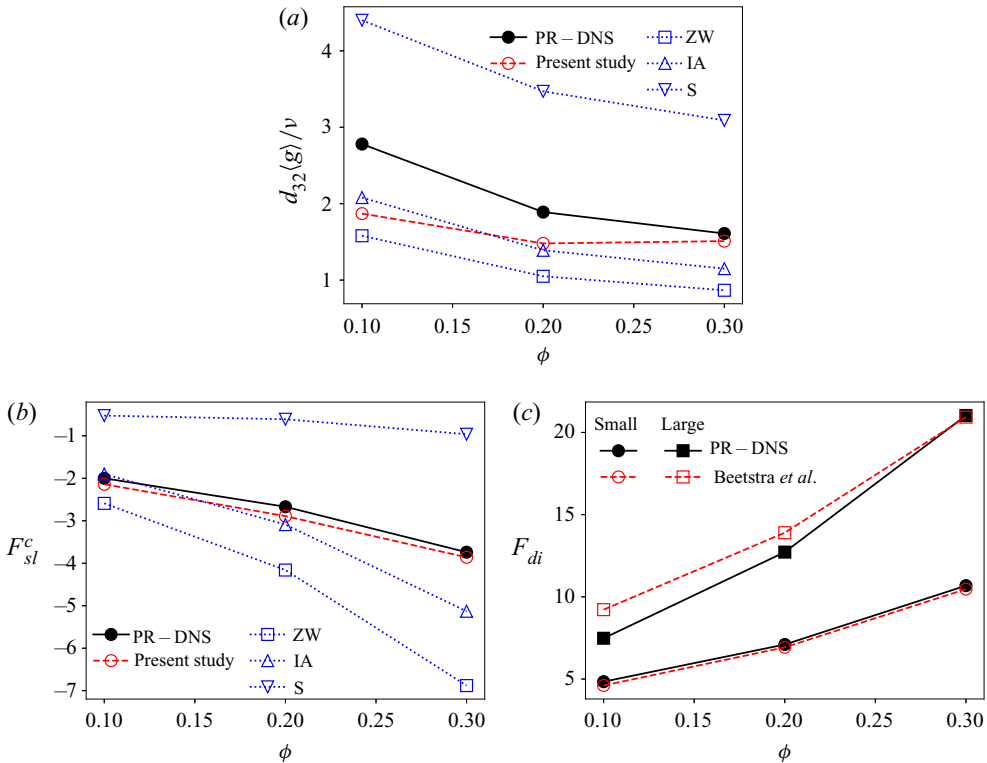


Figure 7. The relative velocity (a), particle–particle drag force of small particles and gas–particle drag force are shown as functions of the total solid volume fraction. Here, the relative velocity is non-dimensionalized by the Sauter mean diameter and kinematic viscosity to give the particle Reynolds number, and the gas–particle drag force is normalized by the Stokes drag force. The abbreviations ZW, IA and S denote the models of Zhao & Wang (2021), Iddir & Arastoopour (2005) and Syamlal (1987), respectively.

by model S is much higher than that of PR-DNSs. As discussed in this paper, model ZW overpredicts the particle–particle drag force by neglecting the correlation between pre-collision velocities and hence underpredicts the relative velocity. The particle–particle drag force predicted by model IA is reasonably good for $\phi = 0.1$ and 0.2 but too high for $\phi = 0.3$. In the derivation process of Iddir & Arastoopour (2005), the Taylor expansion is applied to the Maxwell distribution function and some simplifications are made, such as the module of the relative velocity $|c_i - c_j|$ replaced by $|C_i - C_j|$. The readers can refer to the paper of Zhao & Wang (2020) for more details. In fact, model IA should be the same as model ZW if no approximation is made. A comparison between the predictions of model IA and those of model ZW shows that the approximations made by Iddir & Arastoopour (2005) are inaccurate. Hence the good agreement of model IA for $\phi = 0.1$ and 0.2 is just a coincidence. The model proposed in this study shows good agreement for the particle–particle drag force but underpredicts the relative velocity for $\phi = 0.1$ and 0.2 . The reason for this underestimate is due to the inaccuracy of the gas–particle drag model. As shown in figure 7(c), the model of Beetstra *et al.* (2007) overpredicts the gas–particle drag force of large particles for $\phi = 0.1$ and 0.2 . Since the particle velocity increases with the gas–particle drag force, the large-particle velocity is overestimated, leading to an underestimated relative velocity. This is also the reason why the particle–particle drag forces predicted by model ZW and model IA gradually approach PR-DNSs as ϕ decreases

while the relative velocities do not show this trend. At $\phi = 0.3$, where the model of Beetstra *et al.* (2007) is accurate, the relative velocity predicted by the present model is in good agreement with PR-DNSs, verifying the accuracy of the model proposed in this study.

6. Conclusion

In this work, bidisperse gas–particle suspensions containing smooth particles are simulated by a set of fully resolved methods to examine and improve the particle–particle drag relation derived from KTGF. The computational domain is a small and fully periodic cube that corresponds to a grid in fine MFM simulations. Three total solid volume fractions of 0.1, 0.2 and 0.3 are chosen. The particle Reynolds number ranges from 6.7 to 123.8, and in this range the Stokes number is high so that the lubrication force has a neglectable effect. Under these conditions, the microstructure of the suspensions approaches binary hard-sphere fluids. It is found that the relation derived from the KTGF predicts the collision frequency well but highly overestimates the particle–particle drag force with a mean error of 61 % (maximum 109 %). This is caused by the fact that the pre-collision velocities of colliding particles are not entirely independent of each other. The particle pair that has just collided is likely to collide again after being bounced back by other particles. The interval between the two successive collisions is so short that the post-collision velocities of the first collision cannot relax completely, leading to the pre-collision relative velocity of the second collision being statistically smaller than the domain-averaged relative velocity. Therefore, the KTGF-based relation overestimates the particle–particle drag force when the domain-averaged relative velocity is used.

Considering that a post-collision small particle is bounced back after travelling a mean free path on average, this work proposes to use the relative velocity within spherical shells centred on the centres of large particles and with an outer radius of a mean free path of small particles, to compute the particle–particle drag force. The relative velocity within this local region varies as θ_k , the angle between the vector connecting a particle pair and the flow direction, and its mean is smaller than the domain-averaged relative velocity. In order to consider the anisotropic distribution of the relative velocity, the particle–particle drag forces at different θ_k are first calculated and then summed up. The predictions of this new methodology are in good agreement with simulation results with a mean error of 8 % (maximum 25 %). It is noted that the relative velocity in such a local region cannot be resolved even in fine MFM simulations. For this reason, the effective relative velocity is introduced and fitted as a function of the total solid volume fraction and the volume fraction of small particles based on the predictions of the new methodology. The relation of Zhao & Wang (2021) with this effective relative velocity, i.e. (5.1), can be used in MFM simulations for predictive purposes. It is found by comparing the results of MFM simulations against PR-DNSs that (5.1) shows a significant improvement compared with existing relations in the literature and can give accurate predictions for the relative velocity.

In the present study, the particle surface is assumed to be smooth. However, many particles encountered in nature and industry are frictional. Friction between particles contributes to the particle–particle drag force in two aspects. First, the frictional force is part of the particle–particle drag force when the collision is oblique and the line connecting the particle pair is not parallel with the flow direction. Second, friction enhances energy dissipation. Consequently, the granular temperature decreases, and so does the particle–particle drag force. The relation of Syamlal (1987) only includes the first

Particle–particle drag force

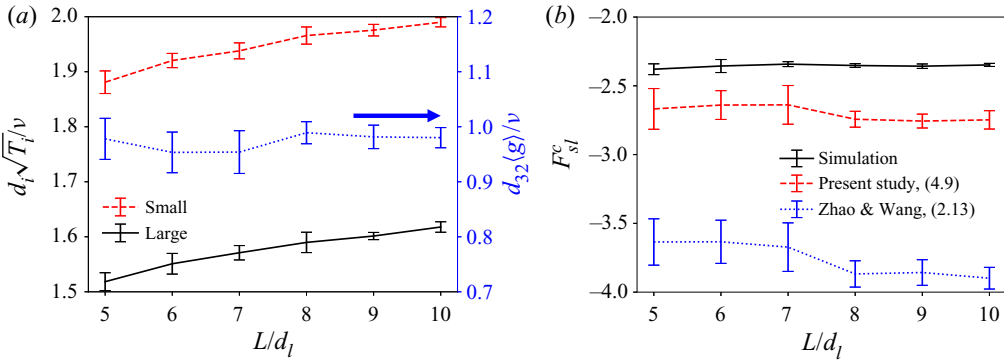


Figure 8. (a) The relative velocity (right axis) and the granular temperature (left axis), in dimensionless form, are plotted as functions of the domain size. (b) The simulated and predicted values of the particle–particle drag force experienced by small particles as functions of the domain size. The error bars in this and the following figure represent the standard deviation for five cases with different initial particle configurations.

aspect by neglecting the granular temperature. It is a non-trivial task to include both two aspects into the particle–particle drag force in a mathematically rigorous way. This is left for future work.

Acknowledgements. We are grateful to the support by the HPC Platform Xi’an Jiaotong University.

Funding. This work was supported by the financial support by the National Natural Science Foundation of China (Grant Nos. 21978228, 51906196).

Declaration of interests. The authors report no conflict of interest.

Author ORCIDs.

Fan Duan <https://orcid.org/0000-0003-4502-9774>;

Qiang Zhou <https://orcid.org/0000-0002-1190-6030>.

Appendix A. The effect of domain size on the particle–particle drag force

To examine the effect of the domain size on the particle–particle drag force, suspensions of $\phi = 0.2$, $x_s \approx 0.1$, $d_l/d_s = 1.6$ and $\langle Re_p \rangle \approx 38.3$ are simulated. The edge length of the computational domains ranges from $5d_l$ to $10d_l$. It is mentioned in § 3 that, for the case of $\phi = 0.3$ and $\langle Re_p \rangle \approx 113.5$, the maximum deviation at the grid size of $d_s/12$, relative to the results at the grid size of $d_s/20$, is just 5.7%. For the case studied in this section, the deviations should be smaller since the required grid resolution decreases as ϕ or $\langle Re_p \rangle$ decreases. Therefore, the grid size of $d_s/12$ is adopted to save computational costs. Figure 8(a) presents the granular temperature and the relative velocity, both in dimensionless form, as functions of L/d_l , which is the ratio of the domain size to the large-particle diameter. It can be seen that, as L/d_l increases, the trend of the relative velocity is unclear, but the granular temperatures of both small and large particles slowly increase. The increase of the granular temperature with domain size was first pointed out theoretically by Cafilisch & Luke (1985) and later evidenced by the simulation results of Ladd (1996). The reason for this increase is still under debate and beyond the scope of this work. The readers can refer to the review of Guazzelli & Hinch (2011) for more information. It should be noted that the suspensions in the previous studies are dilute and in the Stokes regime. The results presented here indicate that the increase of the granular temperature also occurs in dense suspensions at moderate Reynolds numbers.

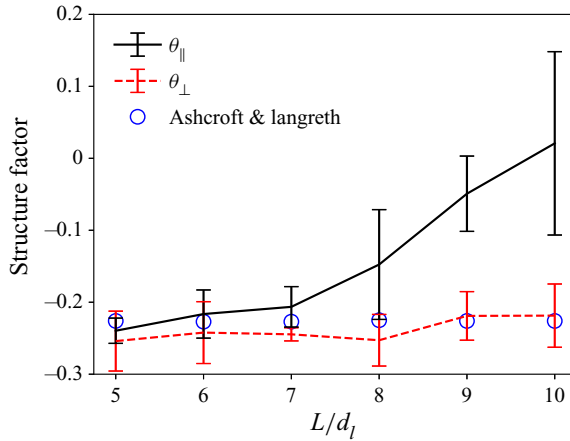


Figure 9. The structure factors of $\kappa = 2\pi/L$ are given as functions of the domain size. Here, θ_{\parallel} and θ_{\perp} are the structure factors in the streamwise and spanwise directions, respectively. For reference, the structure factor predicted by Ashcroft & Langreth (1967) for a binary hard-sphere fluid is given by circles. The slight fluctuation of the theoretical values is caused by the minor change of x_s .

The particle–particle drag force as a function of L/d_l is shown in figure 8(b). The simulated particle–particle drag force barely changes with L/d_l because the increment of the granular temperature is minimal. Both the relation of Zhao & Wang (2021) and the present method using the relative velocity within a mean free path, i.e. $\langle \mathbf{g} \rangle(\theta_k, |\mathbf{r}_s - \mathbf{r}_l| < l_s)$, overestimate the particle–particle drag force, and the overestimation is more severe in the case of $L/d_l > 7$. In the case of $L/d_l \leq 7$, the prediction errors are respectively 55 % and 12 % for Zhao & Wang (2021) and this study, and in the case of $L/d_l > 7$, the prediction errors are respectively 65 % and 17 %, showing a marked improvement.

The increase of the prediction error with the domain size is caused by the inhomogeneity induced by instability. To find the evidence of inhomogeneity, two measures of the particle configuration are calculated and compared with the theoretical values. The first measure is the contact value of the radial distribution function and is used to quantify the short-range structure. It is found that, in the current range of L/d_l , the simulated contact value agrees very well with the formula of Lebowitz (1964), i.e. (2.15), indicating that no short-range change occurs. The second measure is the structure factor between small and large particles and is defined by

$$S_{sl}(\boldsymbol{\kappa}) = \left\langle \frac{1}{\sqrt{N_s N_l}} \sum_{m=1}^{N_s} \sum_{n=1}^{N_l} e^{I\boldsymbol{\kappa} \cdot (\mathbf{r}_{sm} - \mathbf{r}_{ln})} \right\rangle, \tag{A1}$$

where $\boldsymbol{\kappa}$ and I denote the wave vector and the imaginary unit, respectively. Since the instability occurs first for the largest wavelength (the smallest wavenumber) possible, the structure factors of $\kappa = 2\pi/L$ are reported

$$\theta_{\parallel} = S_{sl}(2\pi \mathbf{e}_z/L), \quad \theta_{\perp} = [S_{sl}(2\pi \mathbf{e}_x/L) + S_{sl}(2\pi \mathbf{e}_y/L)]/2. \tag{A2a,b}$$

In this equation, θ_{\parallel} and θ_{\perp} are respectively the structure factors in the streamwise and spanwise directions, and the set of $\{\mathbf{e}_x, \mathbf{e}_y, \mathbf{e}_z\}$ is the basis of a Cartesian coordinate system. The structure factors θ_{\parallel} and θ_{\perp} are also used by Koch & Sangani (1999) to identify inhomogeneous structures. Figure 9 shows the simulated values of θ_{\parallel} and θ_{\perp} as functions of L/d_l . Also shown are the values for a binary hard-sphere distribution, calculated by

the theoretical formula of Ashcroft & Langreth (1967). The theoretical formula is not shown here due to its complex form, and the readers can refer to the original paper of Ashcroft & Langreth (1967) and the paper of Bressel, Wolter & Reich (2015) for more information. As shown in figure 9, the simulated values of θ_{\perp} are in good agreement with the theoretical values, which means that the distribution of the relative position between small and large particles on the horizontal plane is homogeneous. The simulated values of θ_{\parallel} increase with L/d_l and obviously deviate from the theoretical values when $L/d_l > 7$, indicating the critical length scale of the onset of instability for the simulated case is approximately $7d_l$. When clusters are developed, the distributions of the relative velocity and the granular temperature in space are not generally homogeneous. For example, their values are small in a cluster but large at the surface of a cluster (Liu & Hrenya 2018). Therefore, using domain-averaged quantities to calculate the particle–particle drag force is not appropriate. It can be seen from figure 8(b) that our method is more robust than that of Zhao & Wang (2021) in the current range of domain size. This may be attributed to the use of the relative velocity in a local region, the distribution of which should be less affected by the instability.

REFERENCES

- ASHCROFT, N.W. & LANGRETH, D.C. 1967 Structure of binary liquid mixtures. I. *Phys. Rev.* **156**, 685.
- BEETSTRA, R., VAN DER HOEF, M.A. & KUIPERS, J.A.M. 2007 Numerical study of segregation using a new drag force correlation for polydisperse systems derived from lattice-Boltzmann simulations. *Chem. Engng Sci.* **62**, 246–255.
- BENYAHIA, S. 2008 Verification and validation study of some polydisperse kinetic theories. *Chem. Engng Sci.* **63**, 5672–5680.
- BRANDLE DE MOTTA, J.C., BREUGEM, W.P., GAZANION, B., ESTIVALEZES, J.L., VINCENT, S. & CLIMENT, E. 2013 Numerical modelling of finite-size particle collisions in a viscous fluid. *Phys. Fluids* **25** (8), 083302.
- BRESSEL, L., WOLTER, J. & REICH, O. 2015 Particle sizing in highly turbid dispersions by photon density wave spectroscopy: bidisperse systems. *J. Quant. Spectrosc. Radiat. Transfer* **162**, 213–220.
- CAFLISCH, R.E. & LUKE, J.H.C. 1985 Variance in the sedimenting speed of a suspension. *Phys. Fluids* **28**, 759–760.
- CHAO, Z.X., WANG, Y.F., JAKOBSEN, J.P., FERNANDINO, M. & JAKOBSEN, H.A. 2011 Derivation and validation of a binary multi-fluid Eulerian model for fluidized beds. *Chem. Engng Sci.* **66**, 3605–3616.
- CHAPMAN, S. & COWLING, T.G. 1970 *The Mathematical Theory of Non-Uniform Gases: An Account of the Kinetic Theory of Viscosity, Thermal Conduction and Diffusion in Gases*. Cambridge University Press.
- CHEN, Y.P., MEI, Y.F. & WANG, W. 2017 Kinetic theory of binary particles with unequal mean velocities and non-equipartition energies. *Physica A* **469**, 293–304.
- DUAN, F., ZHAO, L., CHEN, X. & ZHOU, Q. 2020 Fluid–particle drag and particle–particle drag in low-Reynolds-number bidisperse gas–solid suspensions. *Phys. Fluids* **32**, 113311.
- FEITOSA, K. & MENON, N. 2002 Breakdown of energy equipartition in a 2D binary vibrated granular gas. *Phys. Rev. Lett.* **88**, 198301.
- FULLMER, W.D. & HRENYA, C.M. 2017 The clustering instability in rapid granular and gas–solid flows. *Annu. Rev. Fluid Mech.* **49**, 485–510.
- FULLMER, W.D., LIU, G., YIN, X. & HRENYA, C.M. 2017 Clustering instabilities in sedimenting fluid–solid systems: critical assessment of kinetic-theory-based predictions using direct numerical simulation data. *J. Fluid Mech.* **823**, 433–469.
- GALVIN, J.E., DAHL, S.R. & HRENYA, C.M. 2005 On the role of non-equipartition in the dynamics of rapidly flowing granular mixtures. *J. Fluid Mech.* **528**, 207–232.
- GARG, R., GALVIN, J., LI, T. & PANNALA, S. 2012 Documentation of open-source MFIx-DEM software for gas–solids flows. https://mfix.netl.doe.gov/doc/mfix-archive/mfix_current_documentation/dem_doc_2012-1.pdf.
- GARZO, V. 2015 Stability of freely cooling granular mixtures at moderate densities. *Chaos, Solitons Fractals* **81**, 497–509.
- GARZO, V. 2019 *Granular Gaseous Flows: A Kinetic Theory Approach to Granular Gaseous Flows*. Springer Nature.

- GARZO, V., DUFTY, J.W. & HRENYA, C.M. 2007 Enskog theory for polydisperse granular mixtures. Part 1. Navier-Stokes order transport. *Phys. Rev. E* **76**, 031303.
- GLANSDORFF, P. 1962 Solution of the Boltzmann equations for strong shock waves by the two-fluid model. *Phys. Fluids* **5**, 371.
- GUAZZELLI, E. & HINCH, E.J. 2011 Fluctuations and instability in sedimentation. *Annu. Rev. Fluid Mech.* **43**, 87–116.
- GUAZZELLI, E. & MORRIS, J. 2012 *A Physical Introduction to Suspensions Dynamics*. Cambridge University Press.
- HILL, R.J., KOCH, D.L. & LADD, A.J.C. 2001 The first effects of fluid inertia on flows in ordered and random arrays of spheres. *J. Fluid Mech.* **448**, 213–241.
- IDDIR, H. & ARASTOPOUR, H. 2005 Modeling of multitype particle flow using the kinetic theory approach. *AIChE J.* **51** (6), 1620–1632.
- JENKINS, J.T. & MANCINI, F. 1987 Balance laws and constitutive relations for plane flows of a dense, binary mixture of smooth, nearly elastic, circular disks. *J. Appl. Mech.* **54** (1), 27–34.
- JENKINS, J.T. & MANCINI, F. 1989 Kinetic theory for binary mixtures of smooth, nearly elastic spheres. *Phys. Fluids A* **1** (12), 2050–2057.
- KOCH, D.L. 1990 Kinetic theory for a monodisperse gas-solid suspension. *Phys. Fluids A: Fluid Dyn.* **2** (10), 1711–1723.
- KOCH, D.L. & HILL, R.J. 2001 Inertial effects in suspension and porous media flow. *Annu. Rev. Fluid Mech.* **33**, 619.
- KOCH, D.L. & SANGANI, A.S. 1999 Particle pressure and marginal stability limits for a homogeneous monodisperse gas-fluidized bed: kinetic theory and numerical simulations. *J. Fluid Mech.* **400**, 229–263.
- LADD, A.J.C. 1996 Hydrodynamic screening in sedimenting suspensions of non-Brownian spheres. *Phys. Rev. Lett.* **76**, 1392.
- LEBOWITZ, J.L. 1964 Exact solution of generalized Percus-Yevick equation for a mixture of hard spheres. *Phys. Rev. A* **133**, 895–899.
- LIU, P. & HRENYA, C.M. 2018 Cluster-induced deagglomeration in dilute gravity-driven gas-solid flows of cohesive grains. *Phys. Rev. Lett.* **121**, 238001.
- LUN, C.K.K. 1991 Kinetic theory for granular flow of dense, slightly inelastic, slightly rough spheres. *J. Fluid Mech.* **233**, 539–559.
- LUN, C.K.K., SAVAGE, S.B., JEFFREY, D.J. & CHEPURNIY, N. 1984 Kinetic theories for granular flow: inelastic particles in Couette flow and slightly inelastic particles in a general flow field. *J. Fluid Mech.* **140**, 223–256.
- MARCHISIO, D.L. & FOX, R.O. 2013 *Computational Models for Polydisperse Particulate and Multiphase Systems*. Cambridge University Press.
- MEHRABADI, M. & SUBRAMANIAM, S. 2017 Mechanism of kinetic energy transfer in homogeneous bidisperse gas-solid flow and its implications for segregation. *Phys. Fluids* **29**, 020714.
- MEHRABADI, M., TENNETI, S. & SUBRAMANIAM, S. 2016 Importance of the fluid-particle drag model in predicting segregation in bidisperse gas-solid flow. *Intl J. Multiphase Flow* **86**, 99–114.
- MONTANERO, J.M. & GARZO, V. 2003 Energy nonequipartition in a sheared granular mixture. *Mol. Sim.* **29**, 357–362.
- NGUYEN, N.Q. & LADD, A.J.C. 2002 Lubrication corrections for lattice-Boltzmann simulations of particle suspensions. *Phys. Rev. E* **66**, 046708.
- SIMEONOV, J.A. & CALANTONI, J. 2012 Modeling mechanical contact and lubrication in direct numerical simulations of colliding particles. *Intl J. Multiphase Flow* **46**, 38–53.
- SOLSVIK, J. & MANGER, E. 2021 Kinetic theory models for granular mixtures with unequal granular temperature: hydrodynamic velocity. *Phys. Fluids* **33**, 043321.
- SONGPRAWAT, S. & GIDASPOW, D. 2010 Multiphase flow with unequal granular temperatures. *Chem. Engng Sci.* **65**, 1134–1143.
- SYAMLAL, M. 1987 The particle-particle drag term in a multiparticle model of fluidization. *Topical Rep. DOE/MC 21353 2373, NTIS/DE 87006500*.
- TSUJI, Y., KAWAGUCHI, T. & TANAKA, T. 1993 Discrete particle simulation of two-dimensional fluidized bed. *Powder Technol.* **77**, 79–87.
- ZAICHIK, L.I., FEDE, P., SIMONIN, O. & ALIPCHENKOV, V.M. 2009 Statistical models for predicting the effect of bidisperse particle collisions on particle velocities and stresses in homogeneous anisotropic turbulent flows. *Intl J. Multiphase Flow* **46**, 38–53.
- ZHAO, L., CHEN, X. & ZHOU, Q. 2021 Inhomogeneous drag models for gas-solid suspensions based on sub-grid quantities. *Powder Technol.* **385**, 170–184.

Particle–particle drag force

- ZHAO, B.D. & WANG, J.W. 2020 A note on the kinetic theory of polydisperse granular flow. *Chem. Engng Sci.* **223**, 115730.
- ZHAO, B.D. & WANG, J.W. 2021 Kinetic theory of polydisperse gas-solid flow: Navier-Stokes transport coefficients. *Phys. Fluids* **33**, 103322.
- ZHOU, Q. & FAN, L.S. 2014 A second-order accurate immersed boundary-lattice Boltzmann method for particle-laden flows. *J. Comput. Phys.* **268**, 269–301.
- ZHOU, Q. & FAN, L.S. 2015*a* Direct numerical simulation of low-Reynolds-number flow past arrays of rotating spheres. *J. Fluid Mech.* **765**, 396–423.
- ZHOU, Q. & FAN, L.S. 2015*b* Direct numerical simulation of moderate-Reynolds number flow past arrays of rotating spheres. *Phys. Fluids* **27** (7), 073306.
- ZHOU, Z.Y., KUANG, S.B., CHU, K.W. & YU, A.B. 2010 Discrete particle simulation of particle-fluid flow: model formulations and their applicability. *J. Fluid Mech.* **661**, 482–510.
- ZHU, H.P., ZHOU, Z.Y., YANG, R.Y. & YU, A.B. 2007 Discrete particle simulation of particulate systems: theoretical developments. *Chem. Engng Sci.* **62**, 3378–3396.